IOP Publishing Superconductor Science and Technology

Supercond. Sci. Technol. **35** (2022) 094008 (13pp) https://doi.org/10.1088/1361-6668/ac86fd

Numerical investigation of current distributions around defects in high temperature superconducting CORC® cables

Reed Teyber[1,*], Maxim Marchevsky[1], Aurora Cecilia Araujo Martinez[1], Soren Prestemon[1], Jeremy Weiss[2,3] and Danko van der Laan[2,3]

[1] Lawrence Berkeley National Laboratory, Berkeley, CA, 94720, United States of America
[2] Advanced Conductor Technologies LLC, Boulder, CO, 80301, United States of America
[3] University of Colorado, Boulder, CO, 80309, United States of America

E-mail: rteyber@lbl.gov

Received 27 April 2022, revised 22 July 2022
Accepted for publication 4 August 2022
Published 19 August 2022

Abstract

High performance ReBCO magnet prototypes are typically monitored and protected with voltage measurements, however a variance in safe operating limits has been observed. A potential issue arises from current redistribution phenomena associated with unidentified defects in cables composed of ReBCO tapes. In this work, a network model is developed to simulate current and voltage distributions around defects in CORC® cables. The evolving network of conductor overlap is evaluated. Trends in CORC® operation at 77 K are presented, and it is shown that power dissipation in an I–V curve depends strongly on a third dimension of defect magnitude. The predictive tool is then coupled with a differential evolution algorithm to recommend optimal CORC® layering topologies based on reel-to-reel tape measurements. The developed model facilitates understanding of CORC® cable phenomena, and the results suggest high temperature superconducting magnet protection can be improved with cable and defect characterization efforts.

Keywords: high temperature superconductor, ReBCO, CORC, fusion, accelerator

(Some figures may appear in colour only in the online journal)

1. Introduction

Magnet technology is poised to benefit from the high-field capabilities of ReBCO high temperature superconducting (HTS) tapes. State-of-the-art magnets based on ReBCO cables [1–3] have been demonstrated [4, 5], however the capital-intensive conductor limits the pace at which ReBCO's potential can be realized [6]. One issue in this development is the unpredictable effectiveness of voltage-based magnet protection, where ReBCO demonstration magnets have been damaged at seemingly benign voltages [7]. New diagnostics and quench detection methods play an important role [8, 9] as well as understanding and mitigating the underlying degradation mechanisms that can lead to resistive transition [10]. Defects, or local reductions in transport performance, are sequentially introduced during tape manufacture, mechanical cabling, magnet fabrication and magnet operation, with bending degradation being most detrimental. The impact of defects on CORC® cables and ultimately HTS magnet operation requires further study, and a model to simulate this behavior is the subject of this work.

* Author to whom any correspondence should be addressed.

Research has been reported on performance degradation throughout the ReBCO life cycle. The field of individual tape characterization is mature, and high-throughput methods are available to measure the spatial variation of tape performance [11, 12]. Several models have been developed to study the mechanics of tape cabling and bending [13–16]. Wang *et al* [5] showed sequential performance reductions in CORC® cable I–V curves from the magnet winding and epoxy impregnation processes, with bending radius resulting in major degradation. A recent study reported performance variations on the order of 15% in tapes extracted from CORC® cyclic load tests [17]. This type of post-mortem analysis has also been performed on solenoid tapes [18] and fusion cables [19].

Knowledge of defects and local performance variations should ultimately be used as inputs to simulations that guide safe operation specific to individual magnets. Electric circuit models [20] and multiphysics models [21, 22] have been developed for HTS cables. Powerful electromagnetic finite element models have also been developed [23, 24], however few resolve current sharing behaviors. In this work, an electric circuit model is developed for CORC® cables. Each tape and the copper core are lumped into lines and discretized along the cable length, and the network of evolving contact areas is evaluated to resolve the tortuous inter-tape current distributions around local reductions in I_c. The impact of defect magnitude on I–V curves is presented with a focus on local power dissipation. The contributions of current sharing and terminal redistribution around defects are explored. The model is then coupled with a differential evolution algorithm to produce optimal layering strategies based on known tape performances. Finally, the implications on cable characterization and magnet operation are discussed.

2. Methods

2.1. CORC® cable geometry

CORC® cables are comprised of layers of helically wound ReBCO tapes. Each layer typically contains 2–3 tapes, and a CORC® cable can contain anywhere from 4 to 30 tapes depending on the application. Sequential layers are counter-wound to minimize inductance, which forms a complex network of overlap between tapes as shown in figure 1. Each tape contacts different tapes in adjacent layers at various points along the winding pitch, and any current transfer to tapes in the same layer must occur either through these neighboring layers or through the termination where current is injected or grounded. This work simplifies the cable modeling by discretizing tapes and the copper core into differential lines with a contact resistance between overlapping tapes.

Each 1D tape is modeled parametrically as a helix:

$$
\begin{aligned}
x &= r_j \cos(t + \beta_j) \\
y &= (-1)^{l_j} r_j \sin(t + \beta_j) \\
z &= P_j t + \psi_j
\end{aligned}
\tag{1}
$$

where t is a parametric variable between 0 and $2\pi n_{\mathrm{turns}}$, r_j is the mean radius of tape j, β creates the offset between tapes in a layer and takes values of $2\pi(0,\ldots,\tau_j-1)/\tau_j$ with τ_j being the number of tapes per layer, l_j is the integer layer number of tape j (co or counter-wound layer), P_j is the winding pitch of tape j and ψ_j is the winding offset (0 in this work). We focus on modeling CORC® geometries that are representative of available experimental samples with low tape counts. In this case, the variation in radius and winding pitch between layers is negligible, and an average value is considered as outlined in table 1.

2.2. Contact resistance matrix

The contact resistance matrix is based on the differential area overlap between two tapes, j and i, at each of k points along the cable length. As shown in figures 1 and 2, the contact area at node k along the cable length is calculated as:

$$
A_{ijk} = \Delta z_j r_j \Delta\theta_{ij}(z_k) \tag{2}
$$

where Δz_j is calculated from the winding pitch (P_j), radius (r_j) and the discretization of the parametric variable t (equation (1)). $\Delta\theta_{ij}(z_k)$ is calculated from the evolving overlapping angular region between tapes (see figures 1 and 2). This considers the differential area as a rectangle aligned with the cable axis.

The procedure undertaken in this manuscript is briefly outlined as follows. Between each tape i, j at each point k, if j is in an adjacent layer to tape i:

- Calculate the angle to the center of each tape, θ_j and θ_i, using the x–y coordinates of equation (1)
- Re-label θ_j and θ_i based on the magnitude of the angles, $\theta_{\min}$, $\theta_{\max}$
- Find the two potential overlapping angles ($\Delta\theta_a$, $\Delta\theta_b$), where $\Delta\theta$ is the angular width of the tape in a z plane passing through point k (see figure 2):

$$
\begin{aligned}
\Delta\theta_a &= (\theta_{\min} + \Delta\theta_{\min}/2) - (\theta_{\max} - \Delta\theta_{\max}/2) \\
\Delta\theta_b &= (\theta_{\max} + \Delta\theta_{\max}/2) - (\theta_{\min} - \Delta\theta_{\min}/2 + 2\pi).
\end{aligned}
$$

- If $\Delta\theta_a < 0$ and $\Delta\theta_b < 0$, there is no overlap and $A_{ijk} = 0$
- Otherwise, $\Delta\theta_{ij} = \max(\Delta\theta_a, \Delta\theta_b)$ and $A_{ijk} = \Delta z_j r_j \Delta\theta_{ij}$

Note that if the adjacent layer is copper core (full exposure), $A_{ijk} = \Delta z_j r_j \Delta\theta_j$. The resulting calculation is shown in figure 3 for the simple case of two layers, two tapes per layer, a single twist pitch and the remaining parameters as defined in table 1. The contact areas increase and decrease linearly, followed by a brief region of no contact over the tape gaps.

2.3. Electric circuit cable simulation

The illustrative electric circuit is shown in figure 4 for a two-layer, two tape-per-layer CORC® cable. The figure is divided into terminal regions (purple background), copper core regions (orange background) and superconducting regions (blue background). The superconducting region contains both superconducting elements (voltage sources with I–V curve) and contact resistances (red resistors). Layer 0 is the outer-most layer,

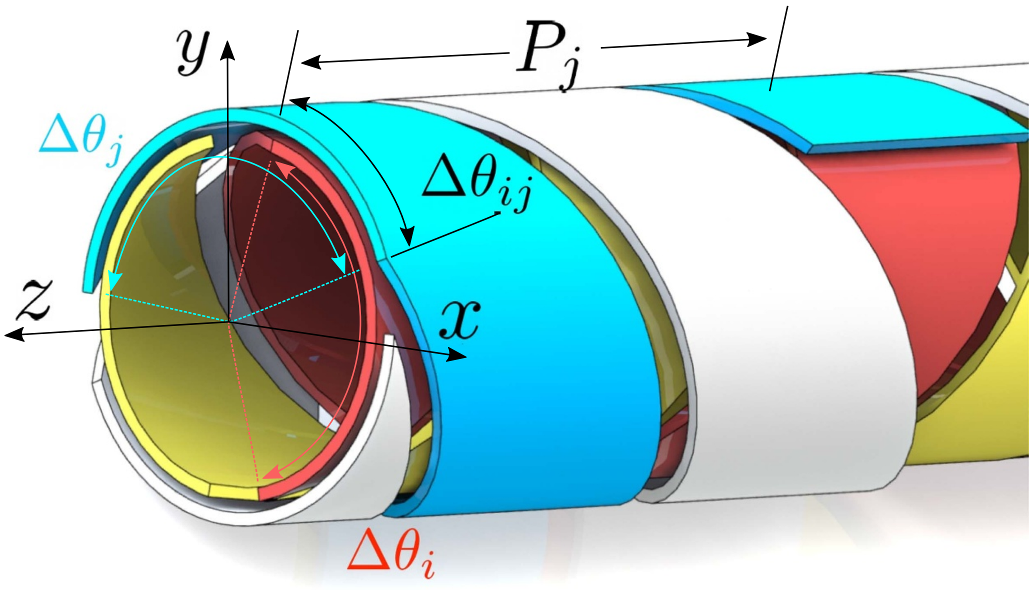

Figure 1. Illustrative four-tape CORC® cable, highlighting the evolving contact areas between tapes. The central copper core is not shown here.

Table 1. CORC® cable parameters.

Parameter	Value
Total number of layers	2
Tapes per layer τ	2
Tape width (mm)	2
Mean radius (mm)	2.75
Mean winding pitch (mm)	5.65
Operating temperature (K)	77
Tape critical current (A)	50
Tape n value (—)	25
Cable length (number of pitches)	350
Differential superconductors per pitch	18
Tape termination resistance (nΩ)	250
Inter-tape contact resistance (nΩ m^2)	3 and 300

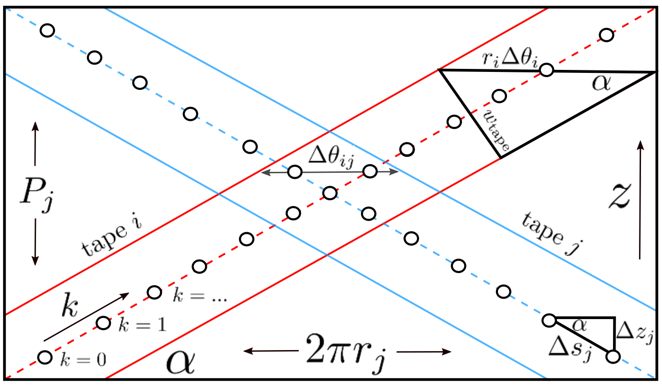

Figure 2. Illustration of overlapping contact areas between two tapes (red, blue) in the context of model parameters.

and layer 1 is the inner-most layer adjacent to the copper core. Although the contact area matrix prohibits a fully realistic network illustration, the contact area evolution is demonstrated for tape 2 in layer 1. At node $k-1$, the tape fully overlaps both the copper core and tape 0; there is no contact with the adjacent tape in the same layer (tape 3, layer 1) or with the remaining tape in the adjacent layer (tape 1, layer 0). At the next point k, tape 2 is in contact with both tapes 0 and 1 in layer 0 in a situation analogous with figure 1. Finally at point $k+1$, tape 2 is only in contact with tape 1 in the adjacent layer.

As done in [20], differential superconducting elements are modeled as power-law voltage sources. The voltage drop between two nodes k and $k+1$ along the cable length is modeled as:

$$\Delta V_{sc,jk} = E_c \Delta s_{jk} \left(\frac{I_{sc,jk}}{I_{c,jk}}\right)^{n_{jk}} \tag{3}$$

where $I_{sc,jk}$ is the current in the superconducting element of tape j at node k, E_c is the electric field criterion of 100 μV m^{-1}, Δs_{jk} is the length of the superconducting element as shown in figure 2, $I_{c,jk}$ is the local critical current of tape j at node k and n_{jk} is the corresponding index value. Equation (3) is assumed to capture the bulk behavior of the tape cross section, however some studies have explicitly modeled the copper stabilizer in parallel with the superconducting layer [21]. This assumption limits our model to cases where the tapes are not driven well above the critical current [25]. All simulated defects consist of a local reduction in I_C across two superconducting elements (1.14 mm). The average power dissipation across a defect (i.e. a 1.14 $\times$ 2 $\times$ 0.1 mm volume for a SCS2050 tape) in W is calculated from the product of differential voltage drop and tape transport current:

$$P_{jk}(z_k) = \Delta V_{sc,jk} I_{sc,jk} \tag{4}$$

which does not consider heating from current sharing. We use equation (4) as a proxy for stability, however a more involved treatment would couple the heat equation with the

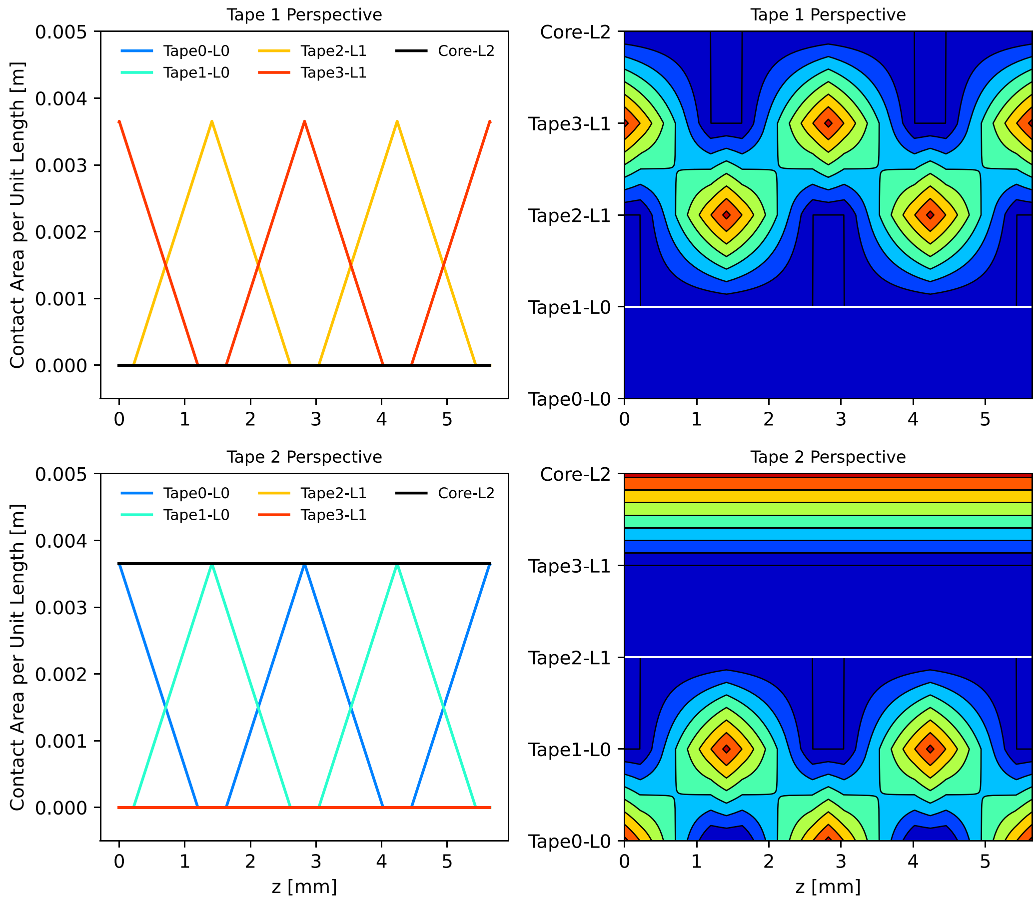

Figure 3. Contours of tape overlap from perspective of tape 1 (top row, outer CORC® layer) and tape 2 (bottom row, inner CORC® layer) over a single twist pitch of a two layer, four tape cable with the parameters of table 1. The naming and layout follow figures 1 and 4. The values in the left column define the contour levels in the right column.

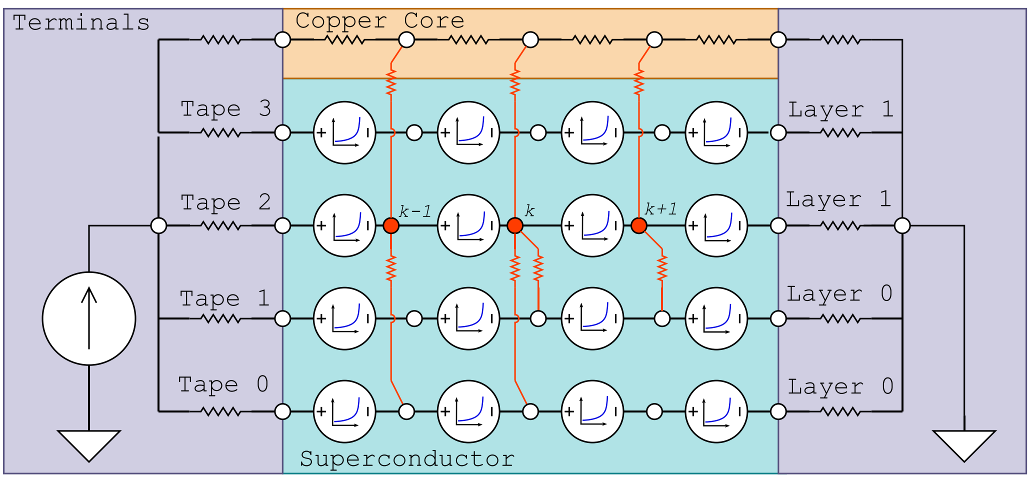

Figure 4. Simplified electric circuit diagram of CORC® cable for a two-layer, four-tape cable. The evolving contact resistance is illustrated only for tape 2 in layer 1.

circuit model. The copper core and contact resistances are calculated as:

$$R_{\text{core}} = \rho_{\text{Cu}} \frac{\Delta z_j}{\pi r_{\text{core}}^2}$$

$$R_{\text{ct},ijk} = \frac{R''_{\text{ct}}}{A_{ijk}} \tag{5}$$

where ρ_{Cu} is the copper resistivity evaluated at 77 K, 0.1 T and $RRR = 100$ (2.15 nΩm). R''_{ct} is the contact resistance (3 and 300 nΩ m^2), a value which spans orders of magnitudes in literature [21, 26, 27], and A_{ijk} is the overlapping area between tapes j and i at node k (see figure 3). The remaining circuit elements are termination resistances (250 nΩ), which have been shown to drive current distributions in short CORC®

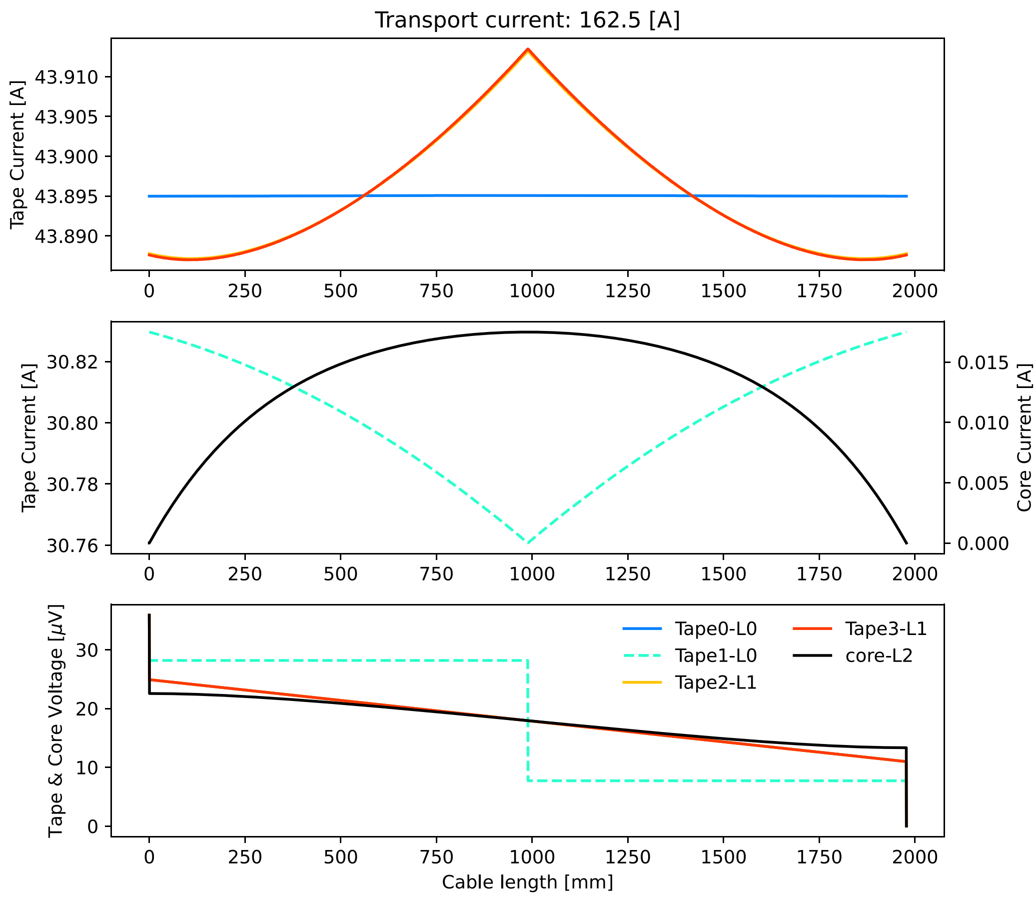

Figure 5. Current (top, middle) and voltage (bottom) distributions of a four-tape, 350 turn cable (1977 mm) with a 50% defect in the middle of tape 1 (middle plot). Simulation is at 162.5 A, 77 K with a contact resistance of 300 nΩ m^2 and a termination resistance of 250 nΩ. Note that the copper core current is on the right y axis of the middle plot. The red curves overlap the yellow curves.

samples [28]. The copper core interfaces only with the superconducting elements; current is not injected directly into the core. The network model is converted into a netlist in Python and solved with NGSPICE.

3. Results

3.1. CORC® current distributions

The impact of defects on current distributions is explored for a 1.977 m CORC® cable at 77 K with the parameters in table 1. Figure 5 shows the current distribution with a local 50% I_C reduction at the midpoint of tape 1 in the outer layer (see figure 4) with an elevated contact resistance of 300 nΩ m^2. The top plot shows the tape currents as a function of length in the three healthy tapes (tape 0, tape 2 and tape 3). The middle plot shows the tape current in the defective tape (tape 1, aqua dashed line on left y axis) and the current in the copper core on the right y axis. The bottom plot shows the voltages as a function of sample length.

At 162.5 A (figure 5), the current distribution is governed by both the termination voltage drop (left and right-most nodes in bottom plot) and the superconductor voltage drop. One might expect each healthy tape to transport the 50 A critical current before the defective tape 1 carries an excess of it is 25 A limiting point. The reality is that the termination resistances create a voltage distribution that promotes a homogeneous current distribution; the defective tape carries 5.8 A more than it is 25 A critical current, while the remaining tapes carry 6.1 A less than their 50 A critical current. This echoes a known consensus that ReBCO cables need low termination resistances to avoid driving tapes into an unsafe regime [28–31].

Figure 6 shows the same scenario as figure 5, however with an increased transport current of 187.5 A; these operating points can be seen on the simulated I–V curve in figure 8. The aggregate sample voltage of 484 μV is now largely comprised of resistive voltage across superconducting elements, with a lower contribution from termination resistances than in figure 5. Figure 7 illustrates the same tape 1 defect at 187.5 A with a reduced contact resistance of 3 nΩ m^2 (from 300 nΩ m^2). The net sample voltage is reduced to 174 μV, and local current sharing is more pronounced. The I–V curves for these samples are shown in figure 8 and summarized in table 2.

3.2. Impact of core properties

The impact of the copper core properties and defective tape location is shown in figure 9 and table 3. The top plot shows I–V curves with low levels of current sharing (300 nΩ m^2) and the bottom plot shows I–V curves with high levels of current

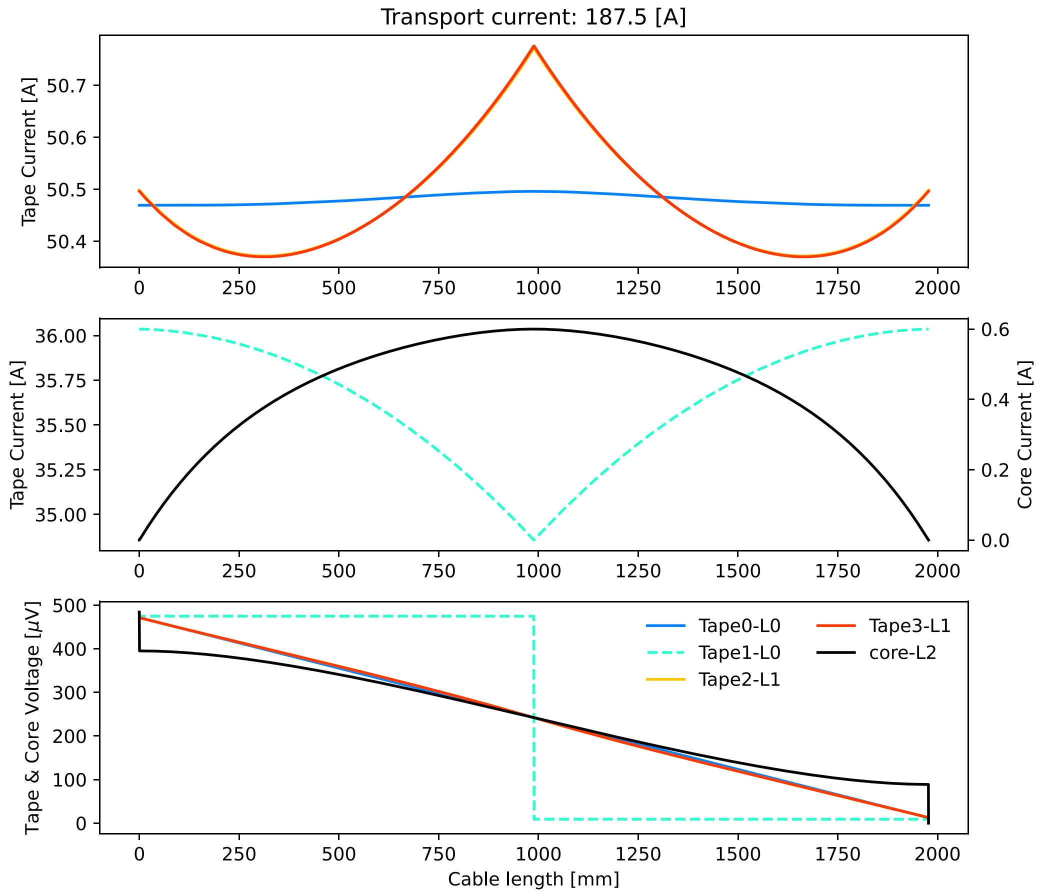

Figure 6. Current (top, middle) and voltage (bottom) distributions of a four-tape, 350 turn cable (1977 mm) with a 50% defect in the middle of tape 1 (middle plot). Simulation is at 187.5 A, 77 K with a contact resistance of 300 nΩ m^2 and a termination resistance of 250 nΩ. The red curves overlap the yellow curves.

sharing (3 nΩ m^2). With high levels of current sharing, the ability to locally share current into a low-resistance copper core makes a noticeable performance improvement as reported in table 3. This is facilitated by both the low resistance copper core (20 K) and by positioning the defective tape next to the copper core (tape 2, see figure 4).

3.3. Impact of defect magnitude

The impact of defect magnitude on cable operation is shown in figures 10 and 11 for contact resistances of 300 nΩ m^2 (low current sharing) and 3 nΩ m^2 (high current sharing), respectively. The top plot shows I–V curves for progressively increasing point defect magnitudes in tape 1, ranging between 50 A (1.0I_C, red) and 25 A (0.5I_C, blue). The bottom plot shows the power dissipation in the 1.14 $\times$ 2 $\times$ 0.1 mm defect volume of the superconductor (equation (4)). Contours of constant voltage are shown on the power dissipation curves based on the total sample voltage. The impact of defects on power dissipation escalates beyond a 20% reduction in I_C, which may be found in magnets with small bend radii. A peculiar effect is observed when the contact resistance is increased to 300 nΩ m^2 (figure 10), where the peak power dissipation for each iso-voltage contour occurs at 0.6I_C; this suggests that there is an optimal-worst defect magnitude. This stems from the combined effects of an altered current distribution and reduced transport current at constant voltage. The non-linear surface of power dissipation, sample voltage and defect magnitude poses a challenge to magnet operators who typically only have access to the magnet I–V curve with little knowledge of defects. Figures 10 and 11 show that there is weak correlation between sample voltage, what magnet operators monitor, and local heat generation pointing to a research need to better characterize defects in HTS cables.

3.4. Impact of defect location

Defects cause current sharing through inter-tape contacts and current redistribution through terminations [32]. Figures 12 and 13 explore the impact of defect location (x axis) and contact resistance (y axis) on the maximum change in termination currents, evaluated as the difference between simulations with and without a 50% defect in tape 1. In all cases, the cable length is held constant while the longitudinal position of reduced critical current is varied. When the transport current is less than the total superconducting capability of the cable,

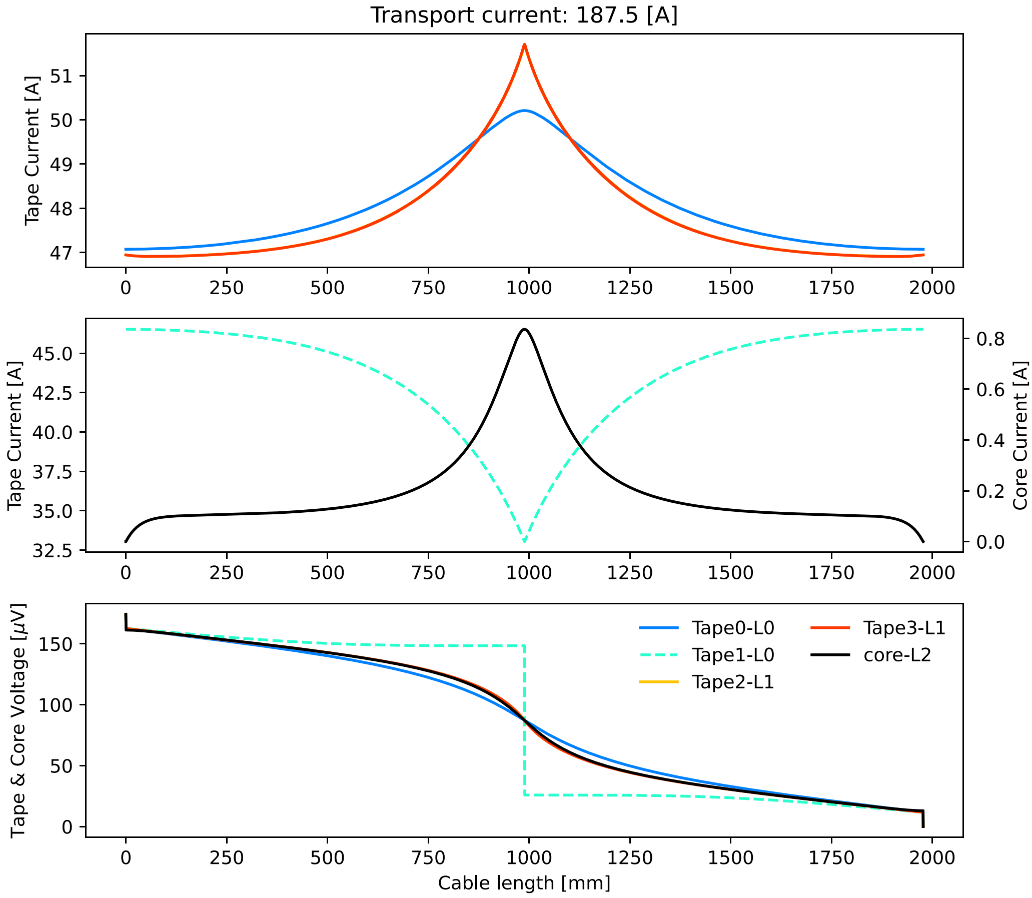

Figure 7. Current (top, middle) and voltage (bottom) distributions of a four-tape, 350 turn cable (1977 mm) with a 50% defect in the middle of tape 1 (middle plot). Simulation is at 187.5 A, 77 K with a termination resistance of 250 nΩ and a reduced contact resistance of 3 nΩ m^2. The red curves overlap the yellow curves.

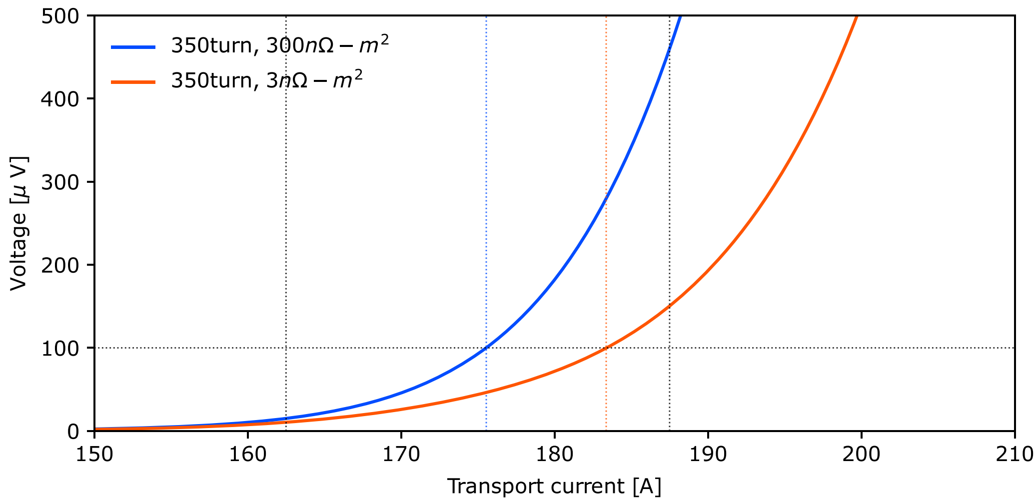

Figure 8. 77 K I–V curves of defective cable (50% I_c in tape 1) with resistive slope removed at two contact resistances. Critical current criteria is shown with horizontal dotted line (table 2). Vertical black lines correspond to transport currents investigated throughout manuscript and vertical colored lines correspond to critical current.

as in figure 12, the 25 A defect in tape 1 causes a large current redistribution that manifests primarily in the terminal. When the operating current is increased to 187.5 A, current tends to redistribute through inter-tape contacts.

3.5. Optimal defect sorting

For the commercial production of CORC® cables, one must choose conductors from a tape inventory and decide where in the cable each tape will lie. If reel-to-reel magnetization

Table 2. I–V fit for curves in figure 8 with resistive slope removed. Curve fit considers current range up to $V_{sample} = 500\ \mu$V.

	$E_c = 1\ \mu\mathrm{V\ cm}^{-1}$		$V_c = 100\ \mu$V	
Case	Ic (A)	n (—)	Ic (A)	n (—)
350 turn, 300 nΩ m^2	180.7	23.2	175.5	23.2
350 turn, 3 nΩ m^2	190.1	18.8	183.4	18.8

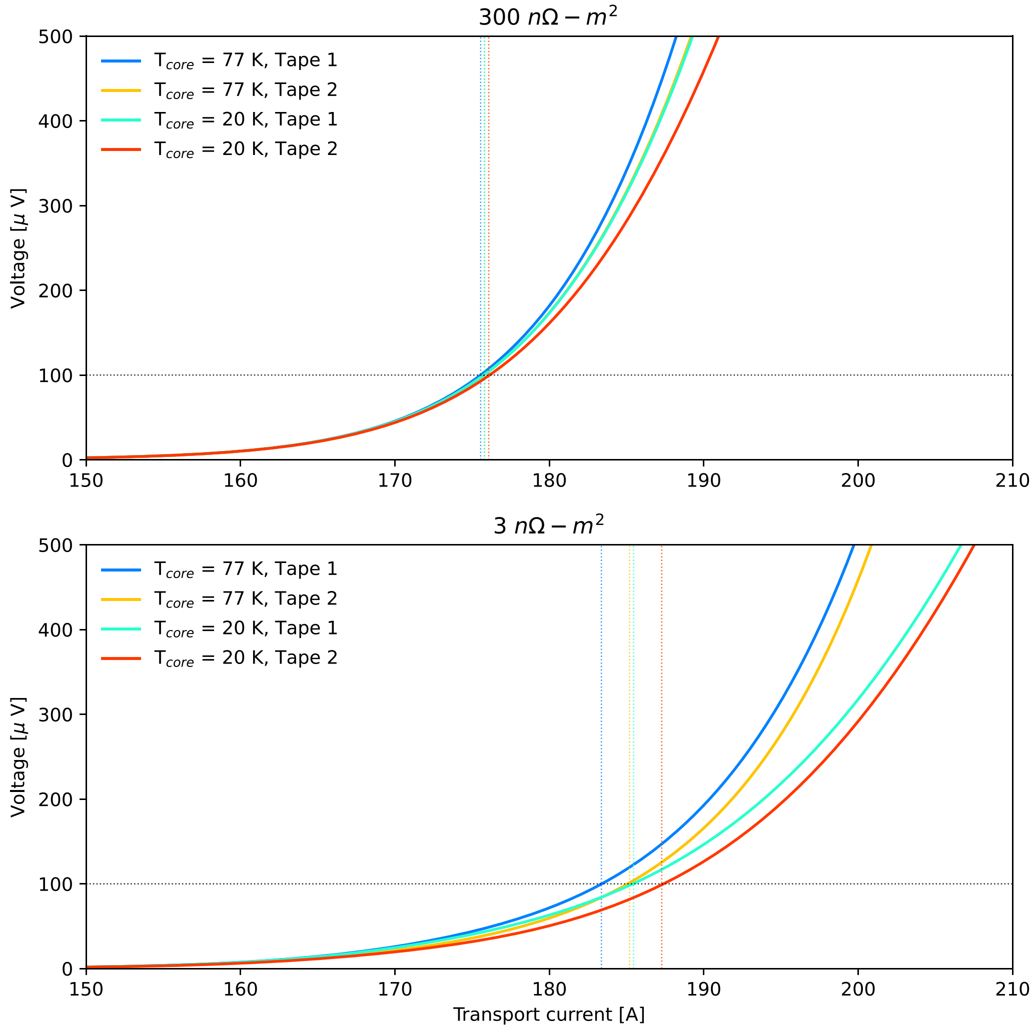

Figure 9. Impact of core resistivity and defective tape on I–V curve with contact resistances of 300 nΩ m^2 (top) and 3 nΩ m^2 (bottom). The critical current fits are reported in table 3.

Table 3. I–V fit for curves in figure 9 with resistive slope removed, showing impact of defective tape and copper core properties on cable performance.

			$V_c = 100\ \mu$V	
R_{ct} (nΩ m^2)	Defect tape (—)	T_{core} (K)	Ic (—)	n (—)
300	1	77	175.5	23.2
300	2	77	175.7	22.0
300	1	20	175.7	21.9
300	2	20	176.0	20.2
3	1	77	183.4	18.8
3	2	77	185.0	19.5
3	1	20	185.3	15.0
3	2	20	187.2	15.9

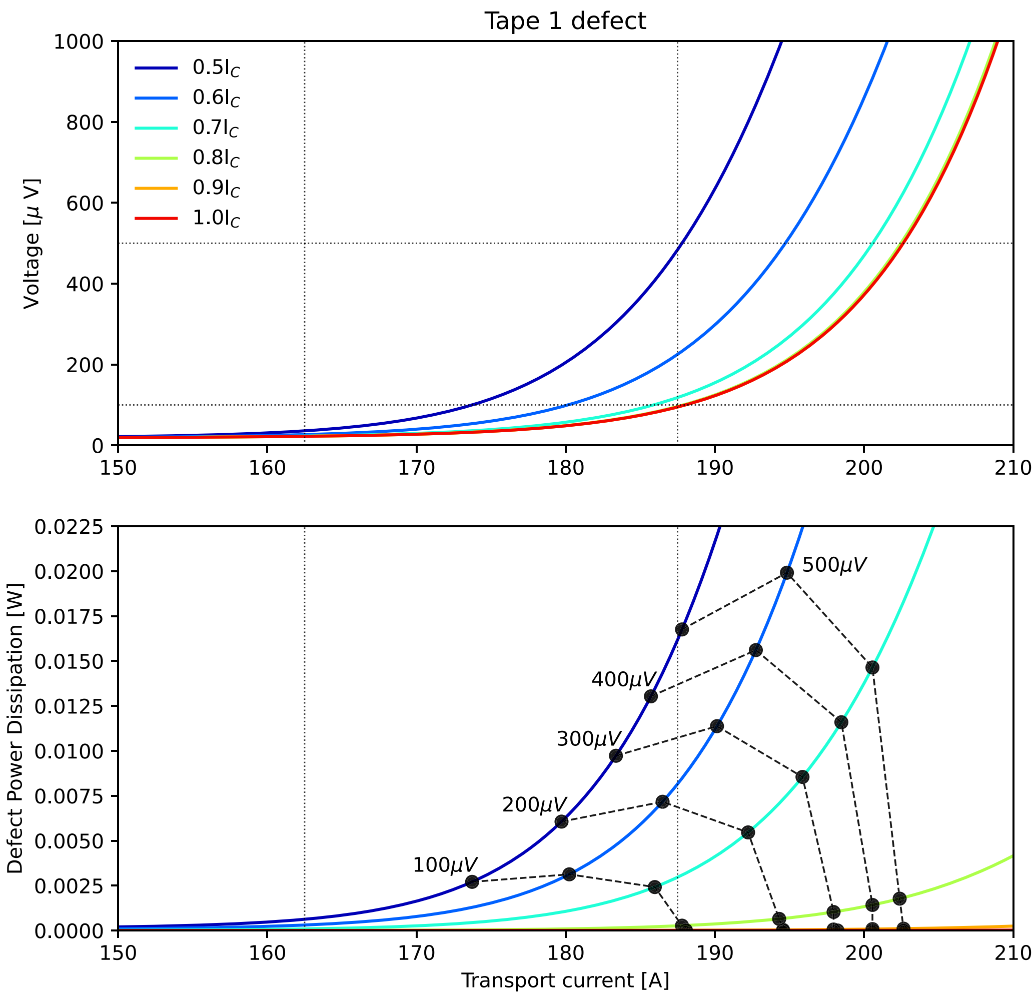

Figure 10. Impact of defect magnitude on I–V curve (top plot) and peak superconductor power dissipation (bottom plot) for a 350 turn cable (1.977 m) with low levels of current sharing (300 nΩ m^2). Contours of constant sample voltage are shown in the power plot, where the power dissipation occurs over a 1.14 $\times$ 2 $\times$ 0.1 mm defect volume. The red curve overlaps the orange and green curves in the top plot.

Table 4. I–V fit for curves in figure 10 with resistive slope removed, showing impact of defect magnitude on cable performance with poor current sharing.

300 nΩ m^2	$V_c = 100\ \mu$V	
Defect (—)	Ic (A)	n (—)
$0.5I_C$	175.5	23.2
$0.6I_C$	182.0	23.3
$0.7I_C$	187.8	24.0
$0.8I_C$	189.9	24.4
$0.9I_C$	190.0	24.4
$1.0I_C$	190.0	24.4

data is available for each tape [11, 12], knowledge of the spatial distribution of local reductions in critical current density can be used to inform layering strategies. In this section, the network model is coupled with an optimization algorithm to recommend the optimal placement and orientation of tapes with defects within a cable. We focus on minimizing the end-to-end voltage of a cable at a desired operating current:

$$\begin{aligned} &\text{Min } V(\vec{\zeta},\vec{\psi})\big|_{I=175\text{A}} \\ &-1 \leqslant \vec{\zeta} \leqslant 1 \\ &-1 \leqslant \vec{\psi} \leqslant 1 \end{aligned} \tag{6}$$

where $\vec{\zeta}$ and $\vec{\psi}$ are design vectors. For a two-layer CORC® cable, consider four tapes with the properties shown in figure 14; two tapes have uniform properties of $I_C = 50$ A, one tape has a 50% defect at 25% of the tape length and the remaining tape has two 50% defects at the midpoint and at 25% of the tape length. The colors correspond to the position of the tape within the cable. The cable layering is defined by two variables for each tape; the integer location within the CORC® cable, ζ, and the orientation of the tape, ψ (i.e. flipping the tape longwise in the cabling machine). For each candidate design in the optimization, tapes are sorted based on ascending values of ψ. Next, any tapes with $\psi \leqslant 0$ have the critical current array

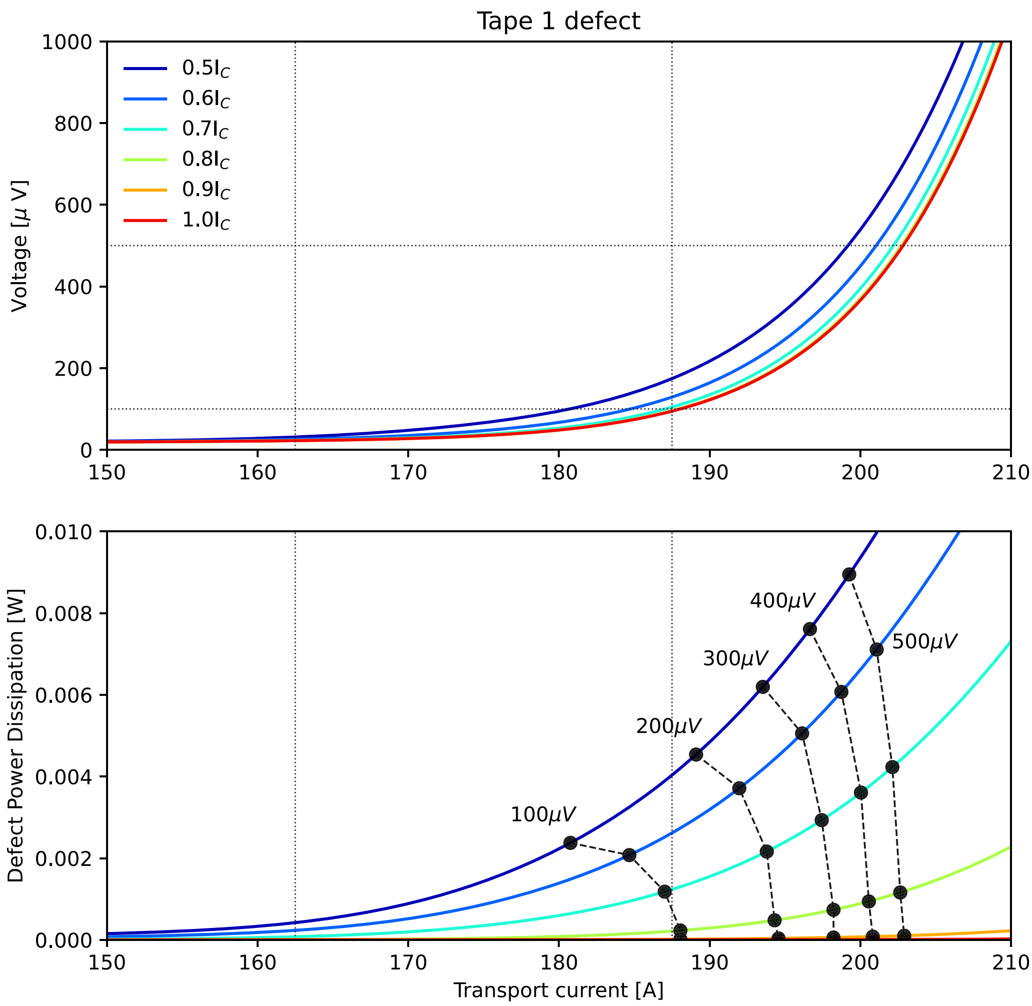

Figure 11. Impact of defect magnitude on I–V curve (top plot) and peak superconductor power dissipation (bottom plot) for a 350 turn cable (1.977 m) with high levels of current sharing (3 nΩ m^2). Contours of constant sample voltage are shown in the power plot, where the power dissipation occurs over a $1.14 \times 2 \times 0.1$ mm defect volume. The red curve overlaps the orange and green curves in the top plot.

Table 5. I–V fit for curves in figure 11 with resistive slope removed, showing impact of defect magnitude on cable performance with high levels of current sharing.

3 nΩ m^2	$V_c = 100\ \mu$V	
Defect (—)	Ic (A)	n (—)
$0.5I_C$	183.4	18.8
$0.6I_C$	187.0	21.6
$0.7I_C$	189.1	23.4
$0.8I_C$	189.9	24.0
$0.9I_C$	190.0	24.1
$1.0I_C$	190.0	24.1

reversed. The resulting critical current matrix is then fed into the simulation process, and the voltage at the single design current of 175 A is returned. The optimization process is solved using the differential evolution algorithm [33].

The optimization results with a contact resistance of 300 nΩ m^2 are shown in figure 14. The minimum voltage configuration is shown in the top plot and the worst configuration is shown in the middle, with the critical current distribution of each tape slightly offset to facilitate visualization. With the parameters of this cable, the results show that the worst performing tapes should be placed in the same layer with the defects spread as far as possible along the cable length. Although the performance improvement is minimal at a conservative voltage criteria of 100 μV, at the 175 A the sample voltage is decreased from 566 to 445 μV with the optimized tape locations.

4. Discussion

The electric field criteria is preferred for cables with uniform tape performance, however this can be misleading when defects or performance variations exist. In this case, the defect can be responsible for the majority of sample voltage while the performance is inflated by normalization across the cable length. If a long cable has a sizeable defect, dangerous levels of power can be dissipated locally before the electric field criteria has been established. This is not a recommendation to abandon the electric field criteria, however; in the absence of large defects, a longer cable will have under-reported performance

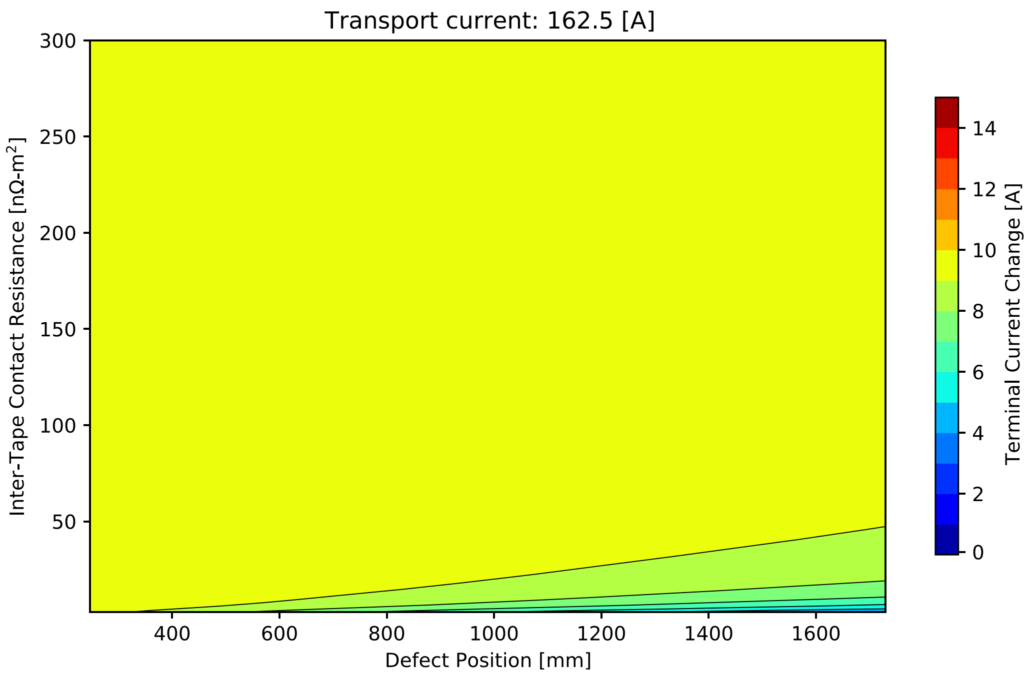

Figure 12. Contours of the terminal current change as a function of the length between defect and terminal (x axis) and the inter-tape contact resistance (y axis) at 162.5 A. Contours show the difference in terminal current between simulations with and without a defect.

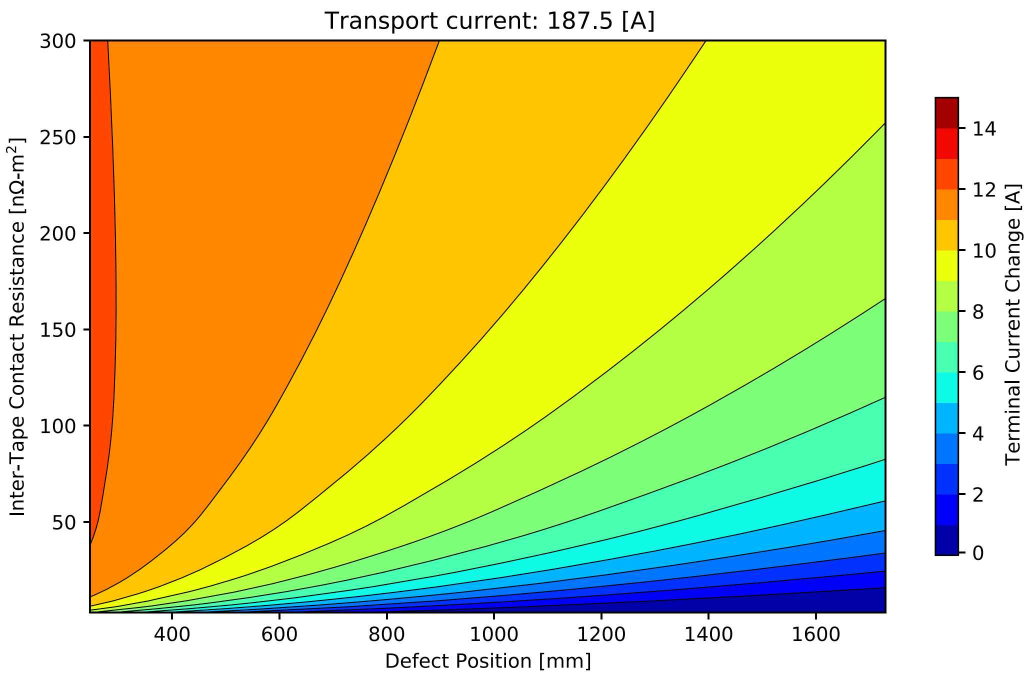

Figure 13. Contours of the terminal current change as a function of the length between defect and terminal (x axis) and the inter-tape contact resistance (y axis) at 187.5 A. Contours show the difference in terminal current between simulations with and without a defect.

with a voltage criteria. The range of transport current considered in an I–V curve can also have an impact on the reported performance of a cable. Neglecting thermal aspects, a cable powered to higher voltage can have a reduced n-value as the linearly resistive copper core plays an increasing role. One should be mindful of these potential shortcomings when reporting cable performance, and when possible, stay consistent with literature.

Most magnets are currently protected with only end-to-end voltage taps. While this can be effective, magnets wound with ReBCO cables have been damaged at voltage levels below what is commonly observed in literature. The results in figures 10 and 11 fit this story; if sizeable defects are present, such as in cables bent to small radii, there can be little correlation between local power dissipation and measured sample voltage. This problem is exacerbated if terminal

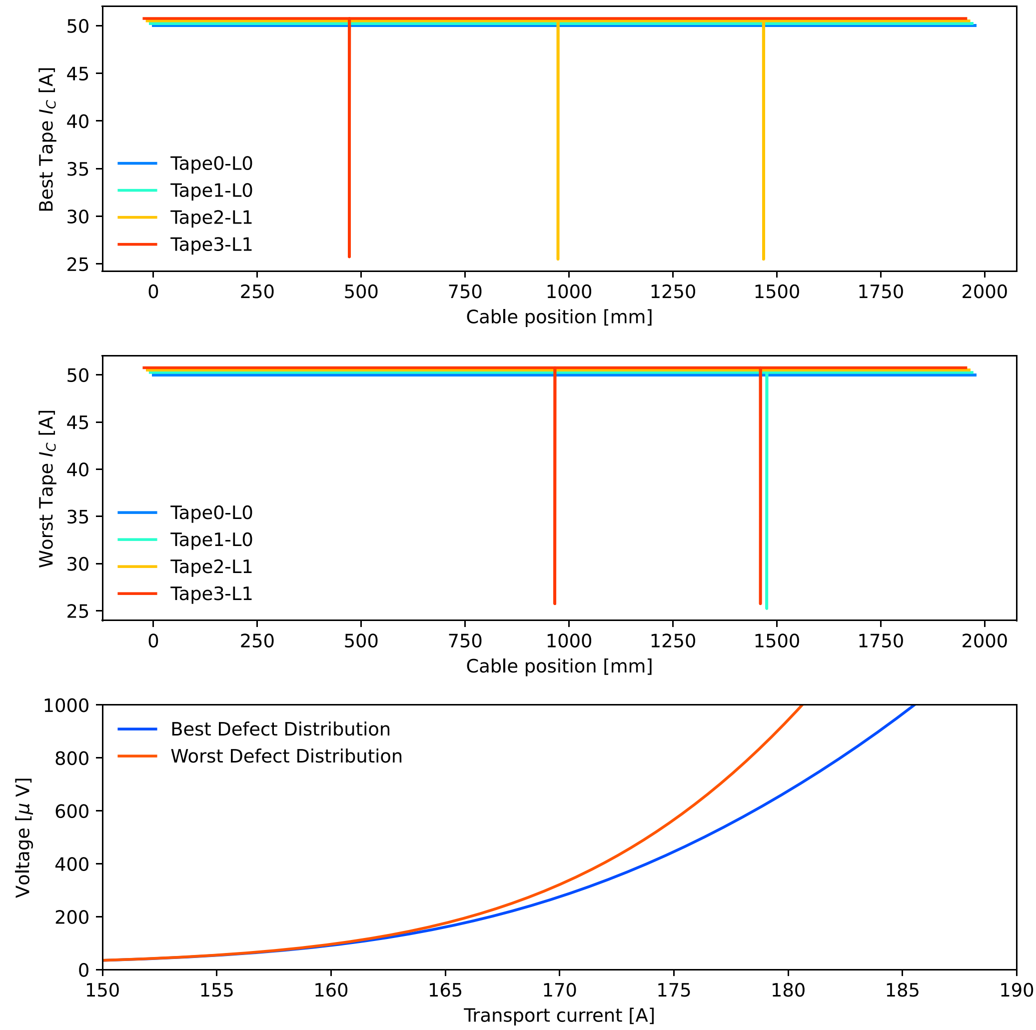

Figure 14. Optimization results showing the best (top) and worst (middle) layering strategies, with the corresponding I–V curves on the bottom. Results are at 77 K with a contact resistance of 300 nΩ m^2 and a 350 turn cable (1.977 m).

resistance maldistribution favors a tape with local defects. Unless magnets are operated below the lowest detectable voltage, which is a function of ramp rate, and with high levels of current sharing, which is typically not known *a priori*, magnet operators are exposing themselves to unpredictable levels of risk. Improved efforts to identify and characterize defects can help operators make more informed decisions with their magnets.

5. Conclusion

A network model is developed to simulate current and voltage distributions around defects in CORC® cables, and the local power dissipation in an I–V curve is shown to be a strong function of the defect magnitude. This suggests that defects need to be characterized to inform safe voltage limits in HTS magnet operation, and suitable methods should be developed. Enhanced current sharing improves cable performance and reduces power dissipation across defects. Future work should couple the developed circuit model with a thermal model to quantify acceptable levels of power dissipation, as well as consider dynamic effects using simplified inductance matrices.

Data availability statement

The data that support the findings of this study are available upon reasonable request from the authors.

Acknowledgments

This work was supported by the US Department of Energy, Office of Fusion Energy Sciences under Grant Number DE-SC0019934.

ORCID iDs

Reed Teyber https://orcid.org/0000-0001-6924-4175
Maxim Marchevsky https://orcid.org/0000-0001-7283-9305
Danko van der Laan https://orcid.org/0000-0001-5889-3751

References

[1] Van der Laan D C, Weiss J D and McRae D M 2019 Status of CORC® wires cables and wires for use in high-field magnets and power systems a decade after their introduction *Supercond. Sci. Technol.* **32** 033001
[2] Hartwig Z S *et al* 2020 Viper: an industrially scalable high-current high-temperature superconductor cable *Supercond. Sci. Technol.* **33** 11LT01
[3] Uglietti D 2019 A review of commercial high temperature superconducting materials for large magnets: from wires and tapes to cables and conductors *Supercond. Sci. Technol.* **32** 053001
[4] van Nugteren J V *et al* 2018 Powering of an HTS dipole insert-magnet operated standalone in helium gas between 5 and 85 K *Supercond. Sci. Technol.* **31** 065002
[5] Wang X *et al* 2021 Development and performance of a 2.9 Tesla dipole magnet using high-temperature superconducting CORC® wires *Supercond. Sci. Technol.* **34** 015012
[6] Wang X *et al* 2022 REBCO–a silver bullet for our next high-field magnet and collider budget? (arXiv:2203.08736)
[7] Wang X *et al* 2018 A viable dipole magnet concept with REBCO CORC® wires and further development needs for high-field magnet applications *Supercond. Sci. Technol.* **31** 045007
[8] Marchevsky M 2021 Quench detection and protection for high-temperature superconductor accelerator magnets *Instruments* **5** 27
[9] Marchevsky M *et al* 2022 Advancing superconducting magnet diagnostics for future colliders (arXiv:2203.08869)
[10] Wang X, Gourlay S A and Prestemon S O 2019 Dipole magnets above 20 tesla: research needs for a path via high-temperature superconducting REBCO conductors *Instruments* **3** 62
[11] Yates Coulter J, Hanisch J, Willis J O, Civale L and Pierce W K 2007 Position and magnetic field angle dependent I_c for long-length coated conductors *IEEE Trans. Appl. Supercond.* **17** 3394–7
[12] Li Y, Chen S, Paidpilli M, Jain R, Goel C and Selvamanickam V 2022 A reel-to-reel scanning Hall probe microscope for characterizing long REBCO conductor in magnetic fields up to 5 Tesla *IEEE Trans. Appl. Supercond.* **32** 1–6
[13] Anvar V A *et al* 2018 Bending of CORC® cables and wires: finite element parametric study and experimental validation *Supercond. Sci. Technol.* **31** 115006
[14] Pierro F, Zhao Z, Owen C M, Colcord C, Chiesa L, Higley H C, Wang X and Prestemon S O 2019 Finite-element analysis of the strain distribution due to bending in a REBCO coated conductor for canted cosine theta dipole magnet applications *IEEE Trans. Appl. Supercond.* **29** 1–5
[15] Wang K, Gao Y, Luo W, Zhou Y and Nijhuis A 2021 Nonlinear contact behavior of HTS tapes during pancake coiling and CORC cabling *Supercond. Sci. Technol.* **34** 075003
[16] Anvar V A, Wang K, Weiss J D, Radcliff K, Van Der Laan D C, Hossain M S A and Nijhuis A 2022 Enhanced critical axial tensile strain limit of CORC® wires: FEM and analytical modeling *Supercond. Sci. Technol.* **35** 055002
[17] Van Der Laan D C, Radcliff K, Anvar V A, Wang K, Nijhuis A and Weiss J D 2021 High-temperature superconducting CORC® wires with record-breaking axial tensile strain tolerance present a breakthrough for high-field magnets *Supercond. Sci. Technol.* **34** 10LT01
[18] Hu X *et al* 2020 Analyses of the plastic deformation of coated conductors deconstructed from ultra-high field test coils *Supercond. Sci. Technol.* **33** 095012
[19] Bykovsky N, Uglietti D, Wesche R and Bruzzone P 2018 Damage investigations in the HTS cable prototype after the cycling test in EDIPO *IEEE Trans. Appl. Supercond.* **28** 1–5
[20] Martínez A C A, Ji Q, Prestemon S O, Wang X and Maury Cuna G H I 2020 An electric-circuit model on the inter-tape contact resistance and current sharing for REBCO cable and magnet applications *IEEE Trans. Appl. Supercond.* **30** 1–5
[21] Van Nugteren J 2016 High temperature superconductor accelerator magnets *PhD Thesis* Twente U., Enschede, Enschede
[22] Kang R, Uglietti D, Wesche R, Sedlak K, Bruzzone P and Song Y 2019 Quench simulation of REBCO cable-in-conduit conductor with twisted stacked-tape cable *IEEE Trans. Appl. Supercond.* **30** 1–7
[23] Krüger P A C, Zermeno V M R, Takayasu M and Grilli F 2015 Three-dimensional numerical simulations of twisted stacked tape cables *IEEE Trans. Appl. Supercond.* **25** 1–5
[24] Wang Y, Zheng J, Zhu Z, Zhang M and Yuan W 2019 Quench behavior of high-temperature superconductor $(RE)Ba_2Cu_3O_X$ CORC® cable *J. Phys. D: Appl. Phys.* **52** 345303
[25] Riva N, Sirois F, Lacroix C, Pellerin F, Giguere J, Grilli F and Dutoit B 2021 A wide range $E-J$ constitutive law for simulating REBCO tapes above their critical current *Supercond. Sci. Technol.* **34** 115014
[26] Lu J, Goddard R, Han K and Hahn S 2017 Contact resistance between two REBCO tapes under load and load cycles *Supercond. Sci. Technol.* **30** 045005
[27] Phifer V, Small M, Bradford G, Weiss J, van der Laan D and Cooley L 2022 Investigations in the tape-to-tape contact resistance and contact composition in superconducting CORC® wires *Supercond. Sci. Technol.* **35** 065003
[28] Willering G P, Van Der Laan D C, Weijers H W, Noyes P D, Miller G E and Viouchkov Y 2015 Effect of variations in terminal contact resistances on the current distribution in high-temperature superconducting cables *Supercond. Sci. Technol.* **28** 035001
[29] Takayasu M, Chiesa L and Minervini J V 2014 Development of termination methods for 2G HTS tape cable conductors *IEEE Trans. Appl. Supercond.* **24** 1–5
[30] Zermeno V, Krüger P, Takayasu M and Grilli F 2014 Modeling and simulation of termination resistances in superconducting cables *Supercond. Sci. Technol.* **27** 124013
[31] Takayasu M, Chiesa L, Allen N C and Minervini J V 2016 Present status and recent developments of the twisted stacked-tape cable conductor *IEEE Trans. Appl. Supercond.* **26** 25–34
[32] Teyber R, Marchevsky M, Prestemon S, Weiss J and van der Laan D 2020 CORC® cable terminations with integrated Hall arrays for quench detection *Supercond. Sci. Technol.* **33** 095009
[33] Storn R and Price K 1997 Differential evolution–a simple and efficient heuristic for global optimization over continuous spaces *J. Glob. Optim.* **11** 341–59